Advanced Functional Materials

ADVANCED FUNCTIONAL MATERIALS
www.afm-journal.de

RESEARCH ARTICLE OPEN ACCESS

Halide Perovskite Integrated Photovoltaic Cathodes Incorporating Pt on ZIF-8-Derived Carbon for Solar Hydrogen Production

Na Yeong Oh[1,2] | Woo Jin Mun[1,2] | Kamran Dastafkan[1] | Matyas Daboczi[1,3] | Hongki Kim[4] | Humza Bhatti[1] | Eunyoung Hong[4] | Minzhi Chen[1] | Yongqi Huang[1] | Jin Hyuk Kim[1,2] | Nicola Gasparini[4] | Jong Hak Kim[2] | Salvador Eslava[1]

[1]Department of Chemical Engineering and Centre of Processable Electronics, Imperial College London, London, United Kingdom | [2]Department of Chemical and Biomolecular Engineering, Yonsei University, Seodaemun-gu, Seoul, South Korea | [3]HUN-REN Centre for Energy Research, Institute of Technical Physics and Materials Science, Budapest, Hungary | [4]Department of Chemistry and Centre for Processable Electronics, Imperial College London, London, United Kingdom

Correspondence: Jong Hak Kim (jonghak@yonsei.ac.kr) | Salvador Eslava (s.eslava@imperial.ac.uk)

Received: 9 April 2026 | **Revised:** 25 June 2026 | **Accepted:** 8 July 2026

Keywords: electrochemical water splitting | hydrogen evolution reaction | IPV-cathode | photocathode | platinum electrocatalyst | ZIF-8

ABSTRACT

Advancing solar-driven hydrogen production in compact, integrated devices requires the development of highly active catalysts with minimal precious-metal loading, alongside light absorbers capable of stable operation in aqueous environments. Here, we report an integrated halide perovskite photovoltaic cathode incorporating a low-Pt-content catalyst supported on zeolitic imidazolate framework-8 (ZIF-8)-derived carbon and a self-adhesive graphite sheet. The ZIF-8-derived carbon, featuring high porosity and surface functional groups from carbonization, enables uniform dispersion of Pt nanoparticles, enhances active-site accessibility, and ensures stability under acidic conditions. As a result, the Pt loading is reduced by an order of magnitude (to 5.60 μg_{Pt} cm^{-2}) while surpassing the catalytic performance of commercial C/Pt (16.0 vs. 26.3 mV overpotential at 10 mA cm^{-2}). The laminated graphite sheet efficiently conducts photoinduced electrons from the photovoltaic layer to the catalyst, provides mechanical support, and prevents electrolyte penetration into the perovskite layers. The resulting monolithic integrated photovoltaic cathode achieves an average photocurrent density of 19.8 mA cm^{-2} at 0.0 V_{RHE} and retains 77% of its initial performance after 160 h of continuous operation in acidic media. These results demonstrate that combining porous carbon-supported low-Pt catalysts with a simple graphite-sheet protection strategy offers a scalable and cost-effective pathway toward durable halide perovskite-based solar hydrogen generation.

1 | Introduction

Coupling light absorption with water-splitting reactions in compact (photo) electrochemical cells offers a sustainable, solar-to-hydrogen production approach [1, 2]. Halide perovskite materials are highly promising candidates in this field because of their excellent light absorption capability [3], tunable bandgap [4], and long carrier diffusion lengths [5]. Despite these remarkable advantages, halide perovskites suffer from a critical drawback: their intrinsic instability in the presence of moisture [6].

Na Yeong Oh and Woo Jin Mun contributed equally to this work.

This vulnerability severely restricts their practical application in direct contact with liquid electrolytes, necessitating effective protection strategies. To overcome this issue, protection and stabilization strategies have been reported, including encapsulation with epoxy sealing [7, 8] and inorganic barrier layers such as Field's metal BiInSn [9, 10], eutectic gallium indium alloy (EGaIn) [11], Ni foil [12, 13], and graphite-epoxy paste [14, 15], coated with various electrocatalysts. Our group developed the use of self-adhesive protective, conductive carbon sheets made of graphite, glassy carbon and boron-doped diamond, moreover coated with Ni and $NiFeO_x$ for halide perovskite integrated photovoltaic anodes (IPV-anodes, arguably also called photoanodes in some contexts) in alkaline media [16–18]. However, this carbon sheet approach remained unexplored for halide perovskite integrated photovoltaic cathodes (IPV-cathodes), despite its potential to offer inexpensive, modular, scalable protection and support for hydrogen evolution reaction (HER) electrocatalysts.

HER in acidic media offers faster reaction kinetics than in alkaline media [19, 20]. HER requires efficient electrocatalysts to minimize overpotential and thereby accelerate hydrogen evolution kinetics. Platinum (Pt) is the most active metal for catalyzing HER in acidic media owing to its nearly optimal hydrogen adsorption-free energy (ΔG_{H^*}), excellent conductivity, and chemical stability [21, 22]. Nevertheless, the high cost and scarcity of Pt hamper its large-scale deployment [23, 24]. Commercial catalysts typically consist of ~20 wt.% Pt supported on carbon (C/Pt). They provide high levels of catalytic activity but offer capital cost challenges for the commercialization of these devices. Although numerous non-precious elements have been explored as cost-effective alternatives, none have yet matched the performance of Pt, which continues to set the benchmark for acidic HER performance [20, 25, 26] Consequently, a key research priority is to drastically reduce Pt loading on catalyst compositions while retaining benchmark activity and durability.

To address the challenge of reducing Pt loading, catalysts must achieve high Pt utilization efficiency by maximizing the exposure of active sites, modulating electronic structure, and optimizing catalyst-support interactions [19, 27, 28]. Various strategies have been investigated, including alloying with transition metals, confining as single-atom catalysts, downsizing to nanoscale, constructing heterostructures, and integrating with advanced supports [29–40]. Among the diverse support materials, metal–organic frameworks (MOFs), crystalline porous structures composed of metal ion centers and coordinated organic linkers, have received considerable attention [41–43]. MOFs offer unique features such as high surface area, tunable porosity, and versatile chemical functionality, which make them highly attractive candidates for developing efficient HER catalysts [44, 45]. Among them, zeolitic imidazolate framework-8 (ZIF-8) is particularly notable due to its well-defined porous structure, chemical stability, and straightforward synthesis method under ambient conditions [46, 47]. Furthermore, ZIF-8-derived carbon obtained by carbonization can preserve ample porosity and provide electrical conductivity and durability. These attributes highlight ZIF-8 and its derivative carbon as a promising platform for the development of HER catalysts. Recent studies have further demonstrated the versatility of MOF-derived carbons and carbon-based functional materials in photovoltaic and energy-conversion applications [48–52].

In this study, we report a monolithic perovskite IPV-cathode that combines an inverted p-i-n perovskite photovoltaic, a protective graphite sheet, and a catalyst of low Pt content supported on ZIF-8 derived carbon. The perovskite absorber layer consists of mixed-cation, mixed-halide $Rb_{0.05}Cs_{0.05}MA_{0.05}FA_{0.85}Pb(I_{0.95}Br_{0.05})_3$. The applied graphite sheet functions as a protective barrier against electrolyte ingress, a robust conductive layer for charge transport, and a mechanical support for the catalyst layer. In addition, the ZIF-8 derived carbon provides highly porous support for Pt particles, ensuring uniform dispersion and enhanced active site accessibility, thereby drastically reducing the Pt loading to 1.8 wt.% (5.60 μg_{Pt} cm^{-2}) while maintaining HER activity comparable to commercial C/Pt of 19.3 wt.% Pt (61.37 μg_{Pt} cm^{-2}). This monolithic IPV-cathode design simultaneously tackles the challenges of Pt scarcity and perovskite instability in aqueous-phase electrochemical operation, reaching average 19.8 mA cm^{-2} of photocurrent density at 0.0 V_{RHE} for solar HER and retaining 77% of its initial performance after 160 h. Consequently, this approach provides a promising platform for IPV-cathodes (arguably also called photocathodes in some contexts) that combines high performance with long-term stability, paving the way toward scalable and cost-effective solar-driven hydrogen production.

2 | Results and Discussion

2.1 | Preparation and Electrocatalytic HER Performance of $C_{ZIF\text{-}8}$/Pt Catalysts

$C_{ZIF\text{-}8}$/Pt catalysts with different Pt loadings were successfully prepared using ZIF-8 particles, H_2PtCl_6, aniline, and a carbonization step at 1100°C under nitrogen environment, as schematically illustrated in Figure 1a. In the first step, ZIF-8 metal–organic framework particles were synthesized by coordinating Zn^{2+} ions and 2MIM in methanol. To introduce Pt species onto the surface of ZIF-8 with enhanced dispersion, ZIF-8 particles were dispersed in an aniline aqueous solution, followed by the addition of H_2PtCl_6 to induce in situ complexation. In this process, aniline coordinates with Pt^{4+} ions, enabling the formation of uniformly distributed Pt-aniline complexes anchored to the porous surface of the ZIF-8 particles, as later confirmed by TEM. In addition, aniline, a weak base, mitigates the strongly acidic environment generated by H_2PtCl_6 (Figure S1), thereby preserving the structural integrity of ZIF-8 during Pt loading. As the amount of H_2PtCl_6 increased, the resulting ZIF-8/aniline/Pt exhibited a distinct color change from light purple to dark purple (Figure 1b). These ZIF-8/aniline/Pt composites were then carbonized under nitrogen flow at 1100°C. This high-temperature treatment not only reduced the organic ligands and framework into conductive carbon but also enabled the sublimation of Zn species, resulting in porous structures with well-dispersed Pt nanoparticles embedded in carbonized ZIF-8 ($C_{ZIF\text{-}8}$) support. ICP-MS was employed to determine the Pt contents in the $C_{ZIF\text{-}8}$/Pt samples, which were 0.05, 0.20, 0.81, and 1.76 wt.%. For comparison, a commercial 20%wt. Pt on carbon catalyst (C/Pt) was measured to contain 19.3 wt.% (labelled C/Pt-19.3%). The Pt loadings of C_{ZIF8}/Pt and commercial C/Pt catalysts, calculated based on a fixed catalyst loaded amount of 0.318 mg cm^{-2}, were determined to be 0.16, 0.64, 2.58, 5.60, and 61.37 μg cm^{-2} for the C_{ZIF8}/Pt and C/Pt samples containing 0.05, 0.2, 0.81, 1.76, and 19.3 wt.% Pt, respectively. In addition, Zn was not detected in any of the samples, confirming

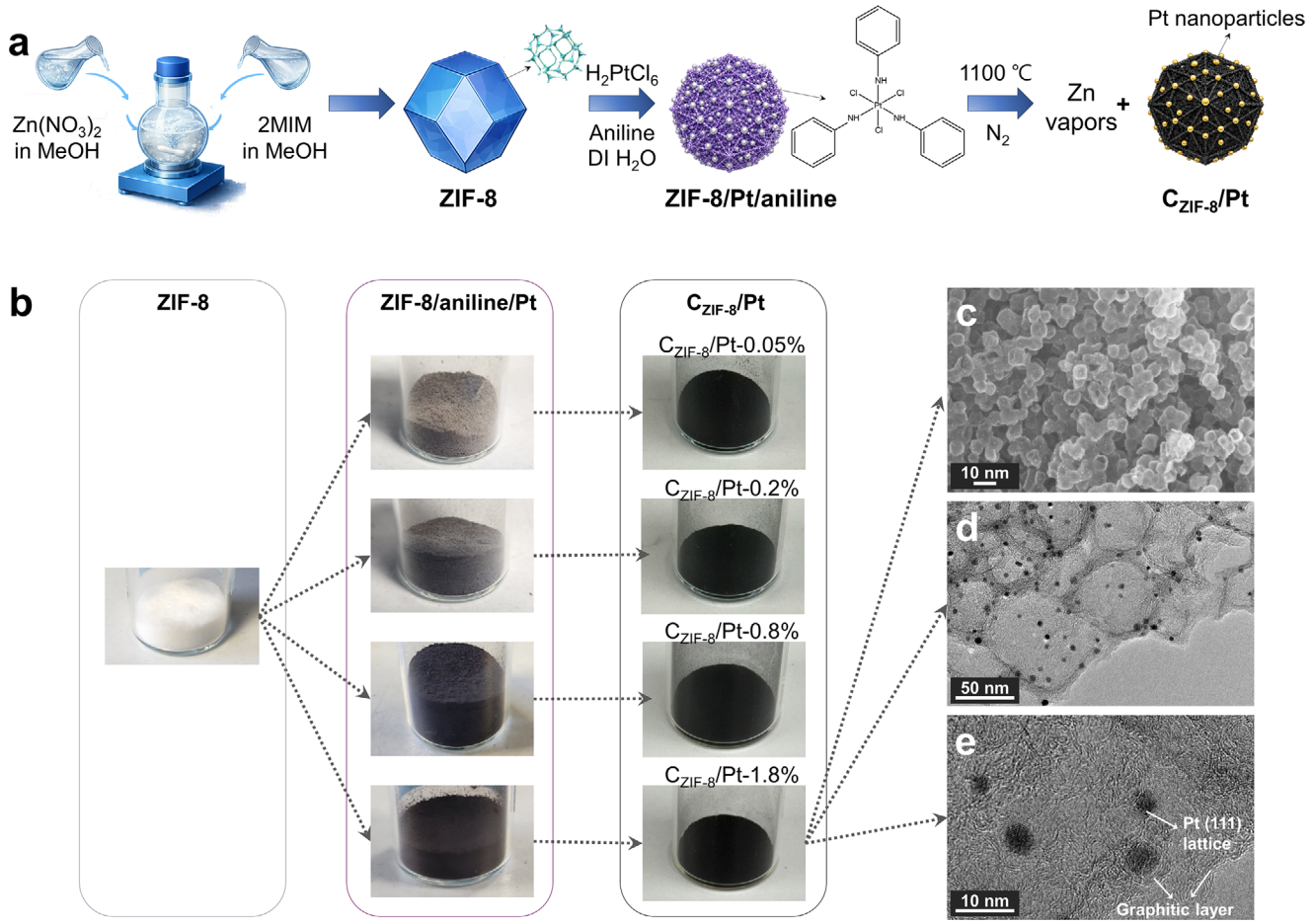

FIGURE 1 | (a) Schematic illustration of the synthesis procedure of $C_{ZIF\text{-}8}$/Pt catalysts. (b) Digital photographs of ZIF-8, ZIF-8/aniline/Pt, and $C_{ZIF\text{-}8}$/Pt. (c) FE-SEM micrograph, (d) TEM micrograph, and (e) high-resolution TEM micrograph of $C_{ZIF\text{-}8}$/Pt-1.8%.

that Zn species were completely evaporated during the high-temperature carbonization process under nitrogen flow. Indeed, Zn was collected downstream the furnace tube at cooler regions.

FE-SEM and TEM micrographs show that the ZIF-8 particles exhibit a uniform polyhedral morphology with sizes ranging from approximately 50 to 100 nm (Figure S2). After anchoring Pt-aniline on the surface of ZIF-8, the edges of ZIF-8/aniline/Pt particles are slightly rounded (Figures S3 and S4). TEM micrographs also confirm this morphological change, exhibiting rounded edges compared to pristine ZIF-8 (Figures S2b and S4a–d). Upon carbonization, $C_{ZIF\text{-}8}$/Pt retains the polyhedral morphology (Figures 1c and S3e–h), but a slight shrinkage in particle size and a hollow structure with carbon shell is observed, due to the loss of volatile species during the carbonization process (Figure S4e–h). This carbon shell must result from the carbonization of the 2MIM linkers and the aniline complexes. In addition, Pt nanoparticles are exposed on the surface of particles, confirming their successful retention and anchoring to the carbon matrix (Figure 1d). TEM-EDS elemental mapping confirms the homogeneous distribution of Pt nanoparticles throughout the carbon matrix, with an average Pt particle size of 3.9 ± 0.8 nm for $C_{ZIF\text{-}8}$/Pt-1.8% (Figure S5). High-resolution TEM analysis displays lattice fringes with a spacing of 0.23 nm, corresponding to the Pt (111) plane (Figure 1e). In addition, well-defined graphitic carbon layers are observed, which can facilitate efficient electron transport to the Pt nanoparticles and improve the stability of catalysts during electrocatalytic reactions by preventing Pt particle agglomeration and dissolution [53, 54].

The electrocatalytic HER activity was evaluated in 0.5 M H_2SO_4 aqueous electrolyte using a three-electrode configuration. The working electrode was prepared via a straightforward drop-casting method, with a catalyst loading of 0.318 mg cm^{-2}. To ensure reliable comparison among samples, measurements were first conducted under conditions free from mass transfer resistance in a rotating disk electrode (RDE). The LSV curves show that the HER activity of the $C_{ZIF\text{-}8}$/Pt catalyst series increases with increasing Pt content (Figure 2a). Remarkably, $C_{ZIF\text{-}8}$/Pt-1.8% exhibits activity comparable to that of the commercial C/Pt-19.3% catalyst, despite containing eleven times less Pt (5.60 vs. 61.37 μg_{Pt} cm^{-2}). The overpotentials at current densities of 10, 20, 50, and 100 mA cm^{-2} (η_{10}, η_{20}, η_{50}, and η_{100}), with each value reported as the average of three independent measurements, decreases with the Pt content (Figure 2b; Figure S6). Among the samples, $C_{ZIF\text{-}8}$/Pt-1.8% delivers the best performance and combination of low overpotential and Pt content (Figure S6), requiring low overpotentials of η_{10} = 16 mV, η_{20} = 32.8 mV, η_{50} = 79.9 mV, and η_{100} = 150.3 mV. Compared with the commercial C/Pt-19.3% catalyst (η_{10} = 26.3 mV, η_{20} = 41.3 mV, η_{50} = 81.3 mV, and η_{100} = 145.7 mV), $C_{ZIF\text{-}8}$/Pt-1.8% shows substantially lower overpotentials at low current densities (η_{10} and η_{20}) and comparable values at

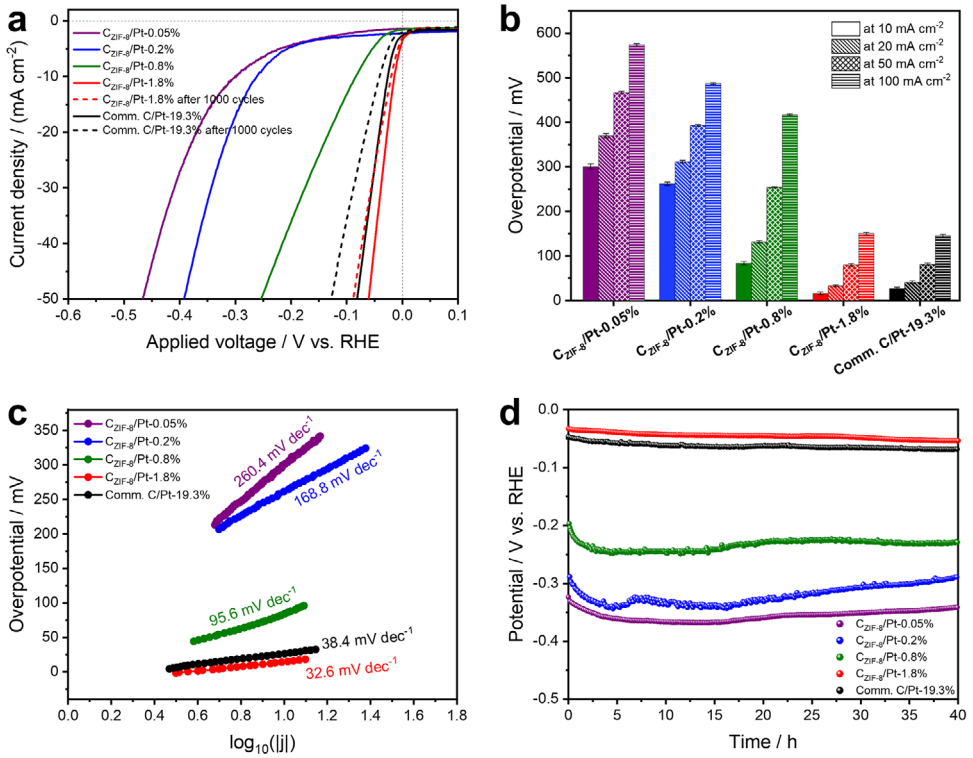

FIGURE 2 | Characterization of commercial C/Pt and $C_{ZIF\text{-}8}$/Pt catalysts: (a) LSV curves, (b) overpotential values at 10, 20, 50, and 100 mA cm^{-2}, (c) Tafel slopes, and (d) chronopotentiometric stability test at 20 mA cm^{-2}. Measurements were conducted using an RDE (2500 rpm) in 0.5 M H_2SO_4. Sweep rate of 10 mV s^{-1}.

higher current densities (η_{50} and η_{100}), underscoring its superior catalytic activity despite the eleven-times lower Pt loading.

To gain further insight, Tafel plots were derived from the LSV curve (Figure 2c). The calculated Tafel slopes for $C_{ZIF\text{-}8}$/Pt-0.05%, $C_{ZIF\text{-}8}$/Pt-0.2%, $C_{ZIF\text{-}8}$/Pt-0.8%, $C_{ZIF\text{-}8}$/Pt-1.8%, and commercial C/Pt-19.3% are 260.4, 168.8, 95.6, 32.6, and 38.4 mV dec^{-1}, respectively. The progressively decreased Tafel slopes with increasing Pt loading suggest improved HER kinetics and activity. $C_{ZIF\text{-}8}$/Pt-1.8% reaches a similar (slightly better) slope than C/Pt-19.3%, confirming enough Pt content and good dispersion of it to match performance [55, 56]. The electrochemical double layer capacitance (C_{dl}) was determined by cyclic voltammetry measurements (Figure S7). The $C_{ZIF\text{-}8}$/Pt catalysts exhibit significantly higher C_{dl} values compared to the commercial C/Pt-19.3%, which shows a C_{dl} value of 7.67 mF cm^{-2}. Specifically, the C_{dl} values of $C_{ZIF\text{-}8}$/Pt-0.05%, $C_{ZIF\text{-}8}$/Pt-0.2%, $C_{ZIF\text{-}8}$/Pt-0.8%, and $C_{ZIF\text{-}8}$/Pt-1.8% are 23.54, 23.11, 21.85, and 19.42 mF cm^{-2}, respectively, showing a gradual decrease with increasing Pt content. The notably enhanced C_{dl} of the $C_{ZIF\text{-}8}$/Pt series indicates that the presence of a larger number of electrochemically accessible active sites, which can be attributed to the highly dispersed Pt nanoparticles and the porous structure inherited from ZIF-8 [57]. The decreasing trend with higher Pt loadings is attributed to the partial surface coverage of the ZIF-8-derived carbon by Pt particles. Nevertheless, $C_{ZIF\text{-}8}$/Pt-1.8% exhibits a large C_{dl} value of approximately 2.5 times greater than that of commercial C/Pt-19.3%, reflecting its higher electrochemically active surface area. To further examine the electrochemical characteristics of Pt, CV measurements were conducted in the extended potential range of + 0.05 to + 0.7 V_{RHE} (Figure S8). However, no distinct hydrogen adsorption/desorption features are observed for $C_{ZIF\text{-}8}$/Pt-1.8%. This behavior is attributed to the ultralow Pt loading and highly dispersed Pt nanoparticles, whose electrochemical response is largely obscured by the substantial double-layer charging current originating from the porous ZIF-8-derived carbon support.

The long-term durability of the catalysts was evaluated by chronopotentiometry at a constant current density of 20 mA cm^{-2} for 40 h using the RDE (Figure 2d). The $C_{ZIF\text{-}8}$/Pt samples with low Pt loadings (< 1 wt.%) exhibits pronounced potential fluctuations during the test. By contrast, $C_{ZIF\text{-}8}$/Pt-1.8% demonstrates excellent stability comparable to the commercial C/Pt-19.3%, with only a 21 mV overpotential increase between the initial and final potentials after 40 h of continuous operation. Durability is further corroborated by comparing the LSV curves before and after 1000 CV cycles (Figure 2a). $C_{ZIF\text{-}8}$/Pt-1.8% shows a minor increase in η_{10} of 5 mV, while commercial C/Pt-19.3% displays a larger overpotential increase of 15 mV after 1000 cycles. Taken together, the low overpotential (η_{10} = 16 mV), small Tafel slope (32.6 mV dec^{-1}), high C_{dl} (19.42 mF cm^{-2}), and robust stability collectively identify $C_{ZIF\text{-}8}$/Pt-1.8% as a highly promising HER catalyst that delivers outstanding activity with eleven times lower Pt content than a commercial benchmark, thereby highlighting its potential as a cost-effective alternative to conventional C/Pt catalysts.

2.2 | Characterization of ZIF-8/Aniline/Pt and $C_{ZIF\text{-}8}$/Pt Catalysts

To gain insights into the HER catalytic activity of $C_{ZIF\text{-}8}$/Pt catalysts, both ZIF-8/aniline/Pt and/or $C_{ZIF\text{-}8}$/Pt catalysts were

characterized by FT-IR spectroscopy, XRD, and Raman spectroscopy. FT-IR spectroscopy confirms that ZIF-8/aniline/Pt was formed (Figure S9a,b). The ZIF-8 particles show three characteristic bands at 3136, 2931, and 1146 cm^{-1}, assigned to stretching vibrations of aromatic C—N, aliphatic C—H, and C—N in the imidazole ring, respectively [57, 58]. These bands are consistently observed in all ZIF-8/aniline/Pt samples, indicating that the incorporation of Pt-aniline complexes does not compromise the structural integrity of the ZIF-8 framework. Additionally, new absorption bands emerge at 3254 and 1588 cm^{-1} upon the introduction of Pt-aniline complexes, corresponding to the N—H stretching and N—H scissoring vibrations of the aniline ligands, respectively [59, 60]. The intensities of these bands appear weaker in the ZIF-8/aniline/Pt samples than in pure Pt-aniline, which is attributed to the thin deposition of Pt-aniline complexes on the ZIF-8 surface. These observations are further supported by XRD analysis (Figure S10), where ZIF-8/aniline/Pt composites display the same characteristic diffraction peaks as ZIF-8. This confirms that the crystallographic structure of ZIF-8 is retained after the deposition of Pt-aniline, suggesting that the presence of the complex does not interfere with the framework ordering. The absence of additional diffraction peaks associated with Pt-aniline is likely due to its relatively low content and amorphous nature.

FT-IR spectra of $C_{ZIF\text{-}8}$/Pt samples and commercial C/Pt-19.3% were obtained to investigate the functional groups in the carbon matrix (Figure S9c). Commercial C/Pt-19.3% does not show any characteristic bands, indicating a highly graphitized carbon support with very low contents of heteroatom functional groups and IR-inactive Pt. By contrast, $C_{ZIF\text{-}8}$/Pt-1.8% exhibits several distinct absorption bands. The absorption bands at 3656, 2981, and 1739 cm^{-1} are assigned to O—H and C—H, and C═O stretching vibrations, respectively, indicating the presence of hydroxyl and carbonyl groups as well as abundant defective edge sites in the carbon matrix [61, 62]. The absorption bands in the range of 1150–1400 cm^{-1} are attributed to C—N, C═N, and C—O stretching vibrations in nitrogen and oxygen functional groups [63, 64]. The presence of these functional groups can enhance the hydrophilicity of the carbon matrix, thereby improving electrolyte accessibility and reducing interfacial resistance. Furthermore, the porous carbon framework containing nitrogen- and oxygen-containing functionalities can facilitate the homogeneous dispersion of Pt nanoparticles, thereby promoting the utilization of catalytically active sites [65].

XRD diffractograms of $C_{ZIF\text{-}8}$/Pt-1.8% and commercial C/Pt-19.3% reveal a broad peak centered around 25° (2θ), which is assigned to the (002) basal plane of graphene layers in a disordered carbon framework (Figure 3a). The peak in $C_{ZIF\text{-}8}$/Pt-1.8% is much broader than in commercial C/Pt-19.3%, indicating higher carbon disorder. Additional diffraction peaks observed at 40°, 46°, and 67° (2θ) correspond to the (111), (200), and (220) planes of Pt (JCPDS No. 04–0802), respectively. These peaks confirm the presence of metallic Pt species in the carbonized composites. Notably, the Pt-related diffraction peaks in $C_{ZIF\text{-}8}$/Pt-1.8% appear sharper than those of commercial C/Pt-19.3%, while maintaining comparable intensity despite its lower Pt content. This indicates that the Pt nanoparticles in $C_{ZIF\text{-}8}$/Pt-1.8% exhibit higher crystallinity, attributed to the thermal annealing at 1100°C, which must facilitate the crystallization and growth of Pt domains.

Raman spectroscopy was employed to evaluate the graphitization degree and structural defects in the catalysts (Figure 3b). All the catalysts exhibit two prominent bands at around 1358 (D band) and 1597 cm^{-1} (G band), corresponding to disordered carbon and graphitic sp^2 carbon, respectively. The intensity ratio of these bands (I_D/I_G) serves as an indicator of structural disorder. In agreement with XRD, the I_D/I_G value of $C_{ZIF\text{-}8}$/Pt-1.8% (1.41) is higher than that of graphite (0.04), confirming the significantly disordered structure. Notably, $C_{ZIF\text{-}8}$/Pt-1.8% shows larger I_D/I_G values compared to commercial C/Pt-19.3% (1.05), indicating a higher degree of defects. The more turbostratic structure of $C_{ZIF\text{-}8}$/Pt-1.8% is attributed to the porous nature of the ZIF-8-derived carbon matrix and the presence of heteroatoms such as nitrogen and oxygen, which are known to disrupt the graphitic lattice and increase defect density. The abundant defects in the ZIF-8-derived carbon matrix can facilitate Pt anchorage and enhance interfacial charge transfer between Pt nanoparticles and the conductive carbon network, thereby improving overall electrocatalytic performance [66].

Nitrogen adsorption and desorption isotherms were obtained to calculate the specific surface area and pore structure of commercial C/Pt-19.3% and $C_{ZIF\text{-}8}$/Pt-1.8% (Figure 3c). The isotherm of $C_{ZIF\text{-}8}$/Pt-1.8% exhibits combined type I/IV curves, characterized by two steep nitrogen uptakes at low ($P/P_0 < 0.01$) and high ($P/P_0 > 0.90$) relative pressure, indicating the presence of micropores (<2 nm) and large (>10 nm) pores and roughness. A noticeable hysteresis loop appears in the range of $0.5 < P/P_0 < 0.9$ for $C_{ZIF\text{-}8}$/Pt-1.8%, revealing the existence of ink-bottle pores, where nitrogen desorption gets blocked in narrow necks until cavitation occurs at ~0.5 P/P_0 [67]. These ink-bottle pores are attributed to the hollow morphology observed by TEM on the $C_{ZIF\text{-}8}$/Pt particles (Figure S4e–h). Further analysis indicates that $C_{ZIF\text{-}8}$/Pt-1.8% exhibits high BET surface area of 498 m^2 g^{-1} and pore volume of 1.8 cm^3 g^{-1}, attributed to the hollow hierarchical pore structure formed upon carbonization (Figure S11). In contrast, commercial C/Pt-19.3% shows significantly lower nitrogen uptake, with a BET surface area of 101 m^2 g^{-1} and total pore volume of 0.47 cm^3 g^{-1}. In addition, the pore size distribution profiles obtained using NLDFT reveals that $C_{ZIF\text{-}8}$/Pt-1.8% possesses two distinct ranges of pore sizes, micropores below 2 nm diameter and meso/macropores of 10–150 nm diameter (Figure 3d) [62, 68]. The <2 nm micropores are attributed to the remaining porosity of ZIF-8 in the particles upon carbonization and the 10–150 nm pores to the intraparticle spaces observed by TEM in the resulting hollow particles. In contrast, commercial C/Pt-19.3% does not exhibit well defined pores, but open larger pores extending to sizes beyond 200 nm attributed to interparticle spaces (Figure 3d). These results show the hierarchical pore structure of $C_{ZIF\text{-}8}$/Pt-1.8%, where different pores can increase surface area and enhance ion and reactant mass transport, which is in line with the improved electrocatalytic performance [69].

XPS was employed to investigate the chemical states of Pt and the surface elemental compositions of the catalysts (Figure 3e,f and Figure S12 and Table S1). The Pt *4f* spectra were deconvoluted in peaks assigned to Pt^0 (71.6 and 74.9 eV), Pt^{2+} (72.5 and 75.9 eV), and Pt^{4+} (74.1 and 77.4 eV) species in both samples. Notably, $C_{ZIF\text{-}8}$/Pt-1.8% exhibits a substantially higher fraction of Pt^{2+} species (58.0%) than commercial C/Pt-19.3% (29.2%), while the

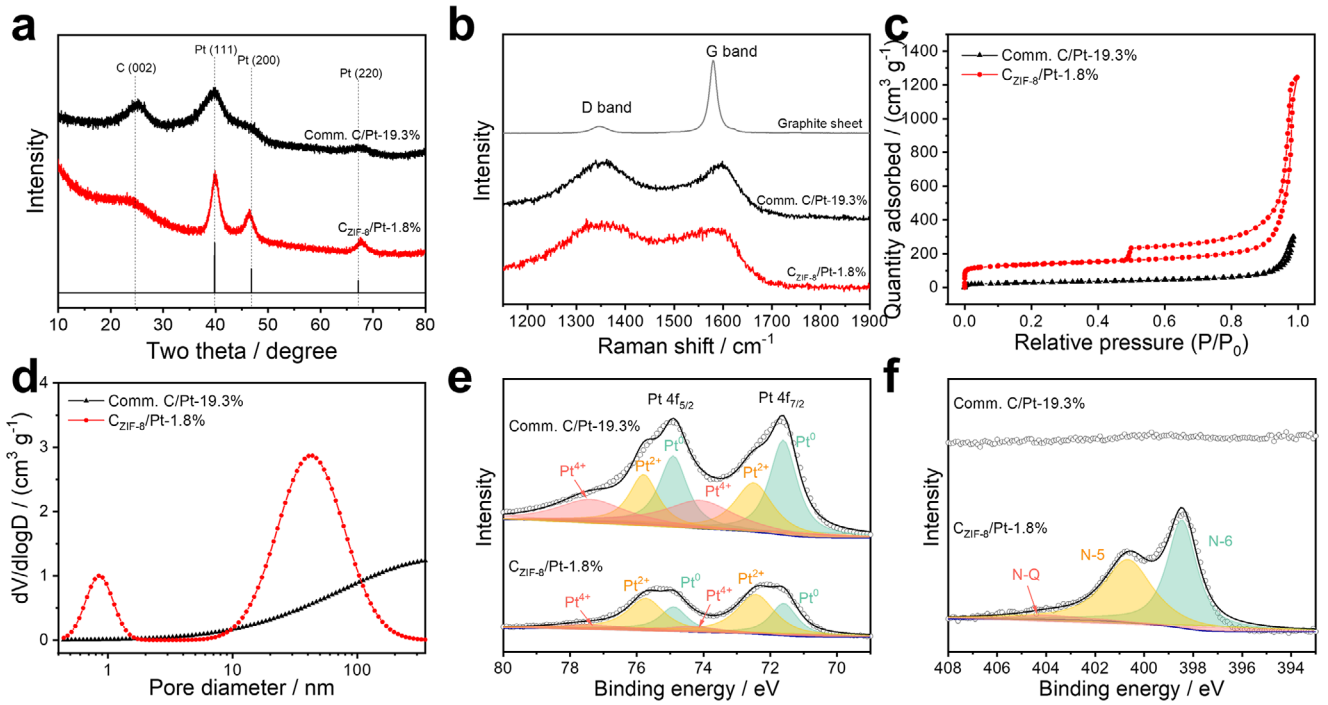

FIGURE 3 | (a) XRD patterns of commercial C/Pt-19.3%, $C_{ZIF\text{-}8}$/Pt-1.8%, and Pt reference pattern (JCPDS card No.04-0802). (b) Raman spectra of commercial C/Pt-19.3%, $C_{ZIF\text{-}8}$/Pt-1.8%, and G15 graphite sheet. (c) N_2 adsorption-desorption isotherms, (d) pore size distributions calculated from the adsorption curve, (e) high-resolution Pt 4f, and (f) N 1s XPS spectra of commercial C/Pt-19.3% and $C_{ZIF\text{-}8}$/Pt-1.8%.

fraction of metallic Pt^0 is lower. The N *1s* spectrum of $C_{ZIF\text{-}8}$/Pt-1.8% confirms the presence of pyridinic N (N-6) and pyrrolic N (N-5) species derived from the ZIF-8 framework and aniline precursor, whereas nitrogen was negligible in commercial C/Pt-19.3%. The coexistence of abundant pyridinic/pyrrolic nitrogen species and a higher Pt^{2+} fraction suggests the presence of Pt—N interactions between Pt species and the nitrogen-rich carbon matrix [70, 71]. Furthermore, the surface Pt content of $C_{ZIF\text{-}8}$/Pt-1.8% was determined to be 0.80 at.%, corresponding to approximately 11.4 wt.%, which is higher than the bulk Pt content measured by ICP-MS. Considering that XPS probes only the outer few nanometers of the material, the higher Pt content determined by XPS indicates surface enrichment of Pt species, which is expected to enhance Pt utilization by improving the accessibility of active Pt sites during the HER process.

2.3 | Graphite-Sheet/Catalyst, PV and IPV-Cathode Performances

Before testing the IPV-cathodes, the HER catalytic performances of $C_{ZIF\text{-}8}$/Pt-1.8% and commercial C/Pt-19.3% on a ~150 μm graphite sheet (G15/$C_{ZIF\text{-}8}$/Pt-1.8% and G15/C/Pt-19.3%) were examined mounted on a glass substrate (without RDE), to ensure consistency with the IPV-cathode measurement. Under this static condition where mass transfer limitation occurs, both catalysts exhibit reduced activity and minor fluctuations in the LSV curves, which are attributed to hydrogen bubble generation and their accumulation on the catalyst surface (Figure 4a). Despite the higher mass transport resistance, G15/$C_{ZIF\text{-}8}$/Pt-1.8% still achieves better performance than G15/C/Pt-19.3%, exhibiting overpotentials of η_{10} = 70 mV and η_{50} = 159 mV, compared with η_{10} = 72 mV and η_{50} = 196 mV for G15/C/Pt-19.3%. In addition, stability was assessed by chronopotentiometry at a constant current density of 20 mA cm^{-2} for 90 h (Figure 4b). G15/$C_{ZIF\text{-}8}$/Pt-1.8% exhibits an overpotential increase of 42 mV between the initial and final values, comparable to the 40 mV increase observed for G15/C/Pt-19.3%. These results confirm that $C_{ZIF\text{-}8}$/Pt-1.8% maintains compelling HER activity and durability even under mass-transfer-limited conditions like those in a static IPV-cathode.

For the photovoltaic component of the IPV-cathode, an inverted (p-i-n) perovskite solar cell was fabricated in which $Rb_{0.05}Cs_{0.05}MA_{0.05}FA_{0.85}Pb(I_{0.95}Br_{0.05})_3$ served as the light-absorbing layer, indium-tin oxide (ITO) as bottom (front with respect to irradiation) contact, MeO-2PACz as the HTL, C_{60}/BCP as the ETL, and Ag and a 30 μm self-adhesive graphite sheet (G3) as the top (rear with respect to irradiation) contact. Representative current density–voltage (*J–V*) characteristics of the fabricated inverted solar cell, featuring a relatively large active area of 0.64 cm^2 are shown in Figure 4c. Under standard AM1.5G illumination (100 mW cm^{-2}), the photovoltaic exhibits a short-circuit current density (J_{SC}) of 23 mA cm^{-2}, an open-circuit voltage (V_{OC}) of 0.91 ± 0.01 V, and a fill factor (FF) of 54% (power conversion efficiency: 11%) under ambient conditions. To evaluate the effect of graphite sheet integration, the photovoltaic performances of the perovskite solar cell without and with G3 and G15/$C_{ZIF\text{-}8}$/Pt-1.8% sheets are compared in Figure S13. Negligible differences are observed, indicating that the graphite sheets and catalyst do not adversely affect photovoltage and photocurrent. Consistently, graphite's work function of approximately −4.55 eV from vacuum, which is slightly deeper than the underlying Ag layer, indicates favourable

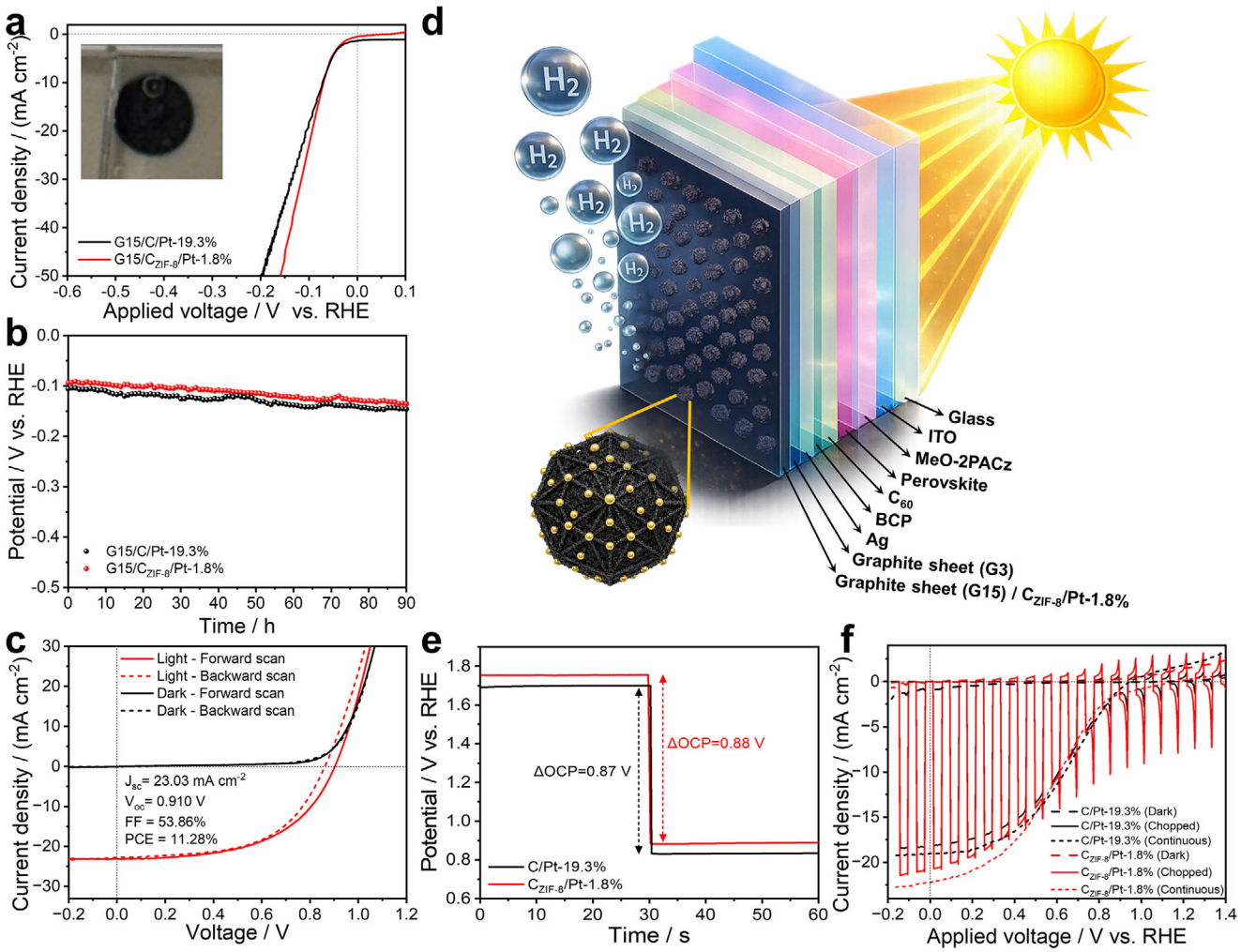

FIGURE 4 | (a) LSV curves and (b) chronopotentiometric stability test at 20 mA cm^{-2} of G15/C/Pt-19.3% and G15/C$_{ZIF-8}$/Pt-1.8% mounted on a glass substrate without RDE. (c) *J–V* curve of the perovskite solar cell incorporating a graphite sheet under forward and reverse bias. (d) Schematic illustration of the monolithic perovskite IPV-cathode structure with its multiple layers. (e) OCP measurements under 1 sun illumination and in the dark (in this order) and (f) LSV curves of IPV-cathodes under dark, continuous 1 sun illumination, and chopped 1 sun illumination. Measurements were conducted in 0.5 M H_2SO_4. Sweep rate of 10 mV s^{-1} under dark and continuous illumination, and 20 mV s^{-1} under chopped-light operation.

energy-level alignment for electron transport (Figure S14) [72, 73]. Current–voltage measurements across an Ag/graphite sheet interface exhibit linear behavior, confirming Ohmic electrical contact and a low resistance of only 0.83 Ω (Figure S15) [17]. This measured resistance would correspond to an estimated voltage loss of only ~12 mV at an operating photocurrent density of 23 mA cm^{-2} in our devices of 0.64 cm^2 active area. These results demonstrate that the graphite sheet functions as an effective conductive layer without introducing significant electrical losses. In addition, this perovskite solar cell, which is highly susceptible to humidity, was relatively stable in ambient humid air with the addition of the G3 graphite sheet as shown in Figure S16 for 160 h, indicating the graphite sheet in practice acts as an encapsulant. Taken together, these results demonstrate that the graphite sheet simultaneously functions as an efficient conductive interlayer and a protective layer in the IPV-cathode architecture.

Next, the monolithic IPV-cathodes were completed by applying the G15/C$_{ZIF-8}$/Pt-1.8% on top of the G3, completing the stack as glass/ITO/MeO-2PACz/Rb$_{0.05}$Cs$_{0.05}$MA$_{0.05}$FA$_{0.85}$Pb(I$_{0.95}$Br$_{0.05}$)$_3$/C$_{60}$/BCP/Ag/G3/G15/C$_{ZIF-8}$/Pt-1.8%, as illustrated in Figure 4d. An equivalent IPV-cathode with commercial C/Pt-19.3% catalyst was also prepared for comparison. The IPV-cathodes were employed as working electrode in a three-electrode electrochemical cell. The change of measured open circuit potential (ΔOCP) in the IPV-cathodes upon switching off the illumination is 0.87–0.90 V, which closely approximates the V$_{OC}$ of 0.91 V of the solar cell (Figure 4c,e; Figure S17a). LSV measurements with continuous and chopped 1-sun illumination are presented in Figure 4f and statistical analysis in Figure S17b. The onset potential of photocurrent is around + 0.9 V$_{RHE}$, measured conservatively by linearly extrapolating the rising of photocurrent. Small dark current and photocurrent spikes are observed before the onset potential of photocurrent (> + 0.9 V$_{RHE}$), assigned to small reactivity with carbon species and capacitive currents. IPV-cathodes with G15/C$_{ZIF-8}$/Pt-1.8% present 19.8 mA cm^{-2} of average photocurrent at 0 V$_{RHE}$, slightly superior to those with G15/C/Pt-19.3% of 17.0 mA cm^{-2} (Figure S17b). The superior average photocurrent density with G15/C$_{ZIF-8}$/Pt-1.8%

is assigned to their better electrochemical results, in agreement with the electrochemical catalyst results. These photocurrent results confirm the integration of the p-i-n perovskite solar cell, protective graphite sheet and $C_{ZIF\text{-}8}$/Pt-1.8% catalyst into a monolithic IPV-cathode.

The transient photocurrents upon light chopping as well as the positive and negative dark currents indicate certain reactivity of the carbon support and/or capacitive currents. To validate this assignment, we compare the electrochemical response of G15/$C_{ZIF\text{-}8}$/Pt-1.8%, G15/C/Pt-19.3%, and a catalyst without carbon support directly electrodeposited Pt on G15 (G15/Pt). Unlike previous dark LSVs (Figure 4a), on this occasion we started at a higher applied potential (+ 1.2 V_{RHE}) to mimic the IPV-cathode LSV measurements and cathodically swept down to −0.1 V_{RHE} (Figure S18). The three samples G15/$C_{ZIF\text{-}8}$/Pt-1.8%, G15/C/Pt-19.3%, and G15/Pt exhibit negative current before the onset of HER (e.g. at + 0.4 V_{RHE}) that we assign to Pt-O reduction and Pt-H formation features [74, 75]. Higher currents are observed for G15/$C_{ZIF\text{-}8}$/Pt-1.8%, followed by G15/C/Pt-19.3%, and it is almost negligible for G15/Pt. This pre-HER current demonstrates carbon reduction, and it agrees with the Raman spectra showing defect (D) band, with intensity decreasing in this order: $C_{ZIF\text{-}8}$/Pt-1.8% > C/Pt-19.3% > G15 (Figure 3c). These LSV curves also suggest enhanced dispersion of Pt particles, since despite larger non-Faradaic currents, Pt-O reduction (+ 0.6 to + 0.9 V_{RHE}) and Pt-H formation features (0 to + 0.2 V_{RHE}) are less pronounced in G15/$C_{ZIF\text{-}8}$/Pt-1.8% compared to those in G15/C/Pt-19.3%.

2.4 | IPV-Cathode Stability and Comparison With the State of the Art

Stability tests of the IPV-cathodes were conducted at a constant potential of 0 V_{RHE} under 1 sun illumination (Figure 5a). The generation of hydrogen during operation was corroborated by visible formation and release of bubbles on the catalyst surface and confirmed by gas chromatography (Figure 5b). For the $C_{ZIF\text{-}8}$/Pt-1.8% IPV-cathode, the photocurrent density decreased from 20 to 16.5 mA cm^{-2} (i.e. to ∼83% of its initial value) after nearly 80 h (t_{80}). At this stage, H_2 bubble accumulation was observed on the surface of the catalyst layer, and replacing the electrolyte led to the recovery of the photocurrent density to its initial value. With continuous operation, the photocurrent density gradually declined again but it still kept a remarkable 15.3 mA cm^{-2} (∼77% of the initial value) at a total operation time of 160 h. Chopping (30 s intervals) of the illumination at this point confirmed the retention of photocurrent response. On the other hand, the IPV-cathode with commercial C/Pt-19.3% shows similar trends but poorer photocurrent density and retention over time, keeping only 10.2 mA cm^{-2} (∼63%) at ∼65 h and 8.5 mA cm^{-2} (∼52%) at ∼160 h. The superior photocurrent density and its retention on the $C_{ZIF\text{-}8}$/Pt-1.8% perovskite IPV-cathode are in agreement with the superior electrochemical performance and stability of $C_{ZIF\text{-}8}$/Pt-1.8% (Figure 2 and Figure S7). For comparison, the stability of the perovskite-based solar cell was evaluated at + 0.2 V for 160 h under 1 sun illumination. The photocurrent density exhibited fluctuations during the continuous tests (first increasing, later decreasing) which can be attributed to slow internal relaxation processes in the halide perovskite, including ionic redistribution and interfacial charge trapping, that dynamically modulate charge transport and extraction [76]; however, even after 160 h, the device remains photoactive, retaining ∼80% of its initial value and demonstrating good operational stability. Based on this solar cell stability test and the previous observations, the photocurrent degradation observed in the IPV-cathode can be attributed to mainly intrinsic degradation of the perovskite-based solar cell and to hydrogen bubble accumulation.

To further examine the stability of the IPV-cathodes, photographs of the electrolyte before and after the stability test were compared (Figure S19). No noticeable visual changes in the electrolyte, such as color variation or detachment of the graphite sheet were detected, suggesting the absence of any severe degradation. Instead, pronounced bubble accumulation was observed on the cell walls and near the catalyst surface, arising from continuous H_2 evolution. Accumulated bubbles adversely influence device performance by blocking the active electrode surface from direct electrolyte contact and imposing local mass transport limitations. These effects account for gradual decline and fluctuations in photocurrent density observed during stability measurements. To further quantify Pt leaching during the stability test, ICP-MS analysis of the electrolyte was performed (Table S2). The dissolved Pt amounts are determined to be 1.02 µg (1.67% of the initially loaded Pt) for commercial C/Pt-19.3% and 0.07 µg (1.26% of the initially loaded Pt) for $C_{ZIF\text{-}8}$/Pt-1.8%. These results indicate that Pt dissolution into the 0.5 M H_2SO_4 electrolyte was negligible for both catalysts during prolonged operation.

Moreover, comparative SEM analyses of G15/C/Pt-19.3% and G15/$C_{ZIF\text{-}8}$/Pt-1.8% before and after the 160 h of stability test were conducted (Figure S20). Prior to the stability test, both catalysts exhibit uniformly coated and densely packed features on the graphite sheet, indicating good adhesion and dispersion of the catalyst layer. After prolonged operation, the catalyst layers show partial surface morphological changes, including localized thinning and variations, which can be attributed to electrolyte-induced swelling and the repeated nucleation and detachment of H_2 bubbles during IPV-cathode operation. However, SEM-EDS elemental mapping of G15/C/Pt-19.3% and $C_{ZIF\text{-}8}$/Pt-1.8% reveal no significant changes in elemental distribution after the stability, indicating that the observed morphological changes are not accompanied by noticeable catalyst redistribution or loss (Figure S21).

To further investigate the structural stability of the commercial C/Pt-19.3% and $C_{ZIF\text{-}8}$/Pt-1.8% catalysts, TEM-EDS elemental mapping and Pt particle size distribution analyses were performed before and after the stability test (Figures S5 and S22). The Pt nanoparticles in both catalysts remain homogeneously distributed throughout the carbon matrix after prolonged operation (Figures S5a,b and S22a,b). The average Pt nanoparticle size of $C_{ZIF\text{-}8}$/Pt-1.8% show negligible change after the stability test (3.9 ± 0.8 nm before testing and 3.4 ± 0.9 nm after testing), whereas Pt particle size of commercial C/Pt-19.3% increase from 2.1 ± 0.4 nm to 3.8 ± 0.8 nm (Figures S5c,d and S22c,d). These results indicate that the ZIF-8-derived carbon matrix effectively suppresses Pt nanoparticle sintering and preserves Pt dispersion during prolonged HER operation.

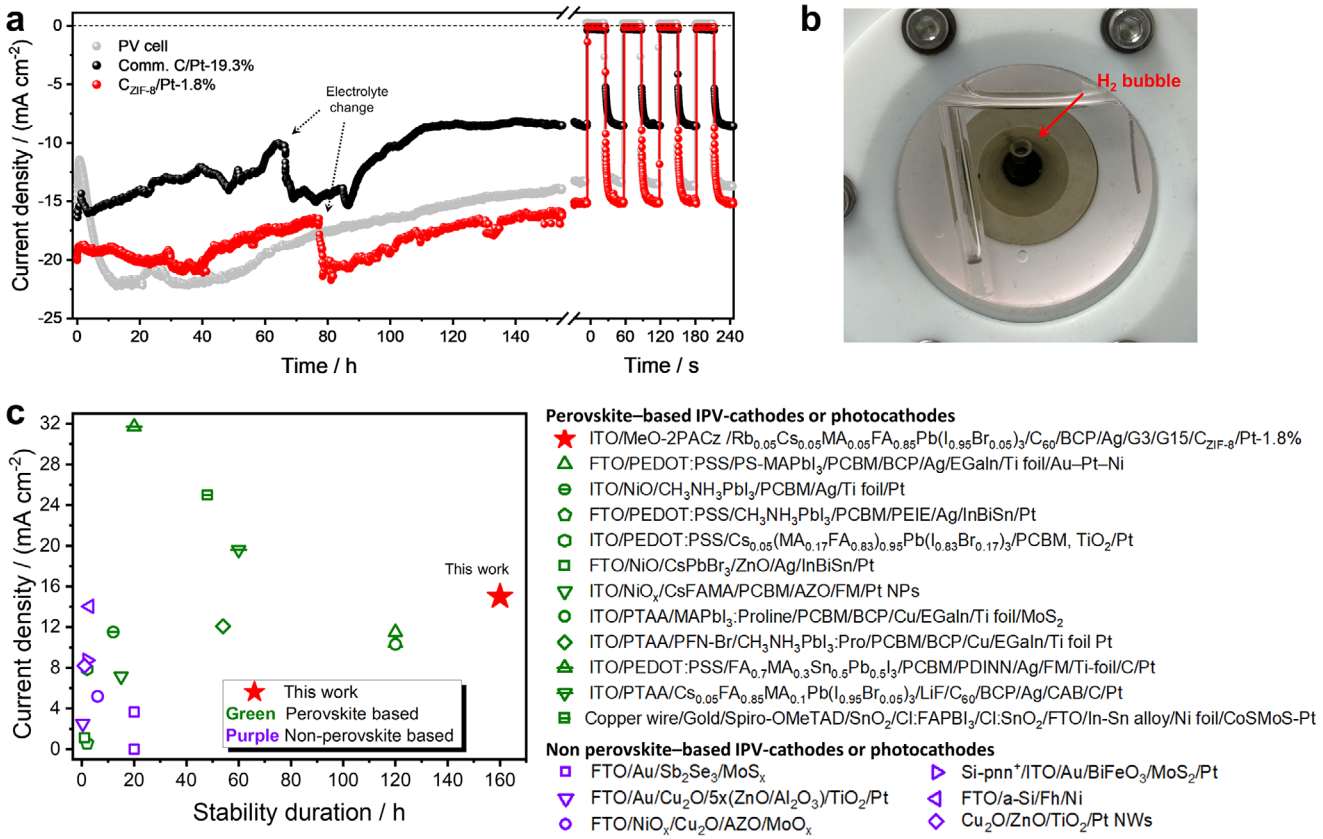

FIGURE 5 | (a) Photocurrent stability test of IPV-cathodes at 0 V_{RHE} for 160 h illumination and photovoltaic at + 0.2 V, both under 1 sun. The electrolyte was replaced at 60–80 h of operation, and the illumination was chopped at 160 h for 30 s on/off intervals. (b) Digital photograph during the stability test showing hydrogen bubble formation. (c) Comparison of stability tests to other photocathodes and IPV-cathodes in literature. The performance parameters and device details are summarized in Table S3.

The photocurrent density maintained by the $C_{ZIF\text{-}8}$/Pt-1.8% perovskite IPV-cathode after 160 h of operation was compared with previously reported IPV-cathodes and photocathodes (Figure 5c and Table S3). The photocurrent density at 0 V_{RHE} applied potential was considered across both perovskite-based [7, 10, 11, 77–84] and non-perovskite-based IPV-cathodes and photocathodes, including Cu_2O [85–87], Sb_2Se_3 [88], a-Si [89], and $BiFeO_3$ [90]. In most of these systems, Pt was employed as the primary catalyst or co-catalyst (as in Au-Pt-Ni and MoS_2/Pt), while some incorporated alternative catalysts such as Ni and MoS_x. Notably, the majority of prior studies evaluated stability over relatively shorter operation times (< 20 h), with one report showing 57% retention after 54 h [11] and another reported retention values of approximately 50% [82], 53% [77], and 67% [77] after 120 h of operation. In contrast, this $C_{ZIF\text{-}8}$/Pt-1.8% perovskite IPV-cathode demonstrates 75% retention even after 160 h, underscoring remarkable long-term durability. This result is particularly noteworthy given the vulnerability to moisture and water of halide perovskites. Halide perovskites are highly susceptible to degradation, severely limiting their applicability in liquid-phase systems. Graphite sheets are herein demonstrated to serve both as a protective barrier against electrolyte permeation and as support for HER catalyst layer. Moreover, $C_{ZIF\text{-}8}$/Pt catalyst is found effective at reducing the Pt loading, leveraging the high surface area derived from the carbonization of ZIF-8 to boost HER activity.

3 | Conclusion

We demonstrate a halide perovskite monolithic integrated photovoltaic cathode (IPV-cathode) that uses a low-content-Pt (1.76%wt., 5.60 μg_{Pt} cm^{-2}) electrocatalyst supported on ZIF-8-derived carbon and a commercially available graphite sheet to simultaneously address the challenges of reducing Pt utilization and mitigating the intrinsic instability of halide perovskites in (photo) electrochemical liquid-phase systems. The derived $C_{ZIF\text{-}8}$/Pt-1.8% catalyst, synthesized via an anchoring step with Pt-aniline complex, exhibits a low overpotential of 16 mV at 10 mA cm^{-2} and demonstrates long-term stability comparable to commercial ~20 wt.% Pt supported on carbon (C/Pt). The porous structure, inherited from ZIF-8, enables highly dispersed Pt nanoparticles with enhanced active site accessibility, thereby delivering excellent hydrogen evolution reaction (HER) activity with eleven times less Pt loading. For IPV-cathode fabrication, a conductive graphite sheet was incorporated through a straightforward lamination process. The graphite sheets play multiple roles in the IPV-cathode architecture: (i) conductive layer to transfer the photoinduced electrons, (ii) effective protective barrier to prevent electrolyte penetration into the perovskite during HER, and (iii) mechanical support for the $C_{ZIF\text{-}8}$/Pt-1.8% HER catalyst loaded by drop casting. With this straightforward yet effective integration, the perovskite monolithic IPV-cathodes achieve photocurrents around 20 mA cm^{-2} at 0 V_{RHE} and onset

potential of + 0.9 V_{RHE} and retain 77% of its initial photocurrent density after 160 h of operation, demonstrating remarkable long-term stability under acidic solar HER conditions. These findings underscore a practical and scalable route for fabricating efficient perovskite-based cathodes, offering a promising pathway toward cost-effective and sustainable solar-driven hydrogen production.

4 | Experimental Section

4.1 | Materials

Zinc nitrate hexahydrate ($Zn(NO_3)_2{\cdot}6H_2O$, 98%), 2-methylimidazole (2MIM, 99%), chloroplatinic acid solution (H_2PtCl_6, 8 wt.% in H_2O), aniline (99%), Aquivion D79-25BS (Aquivion, 25% in water), potassium hexachloroplatinate (K_2PtCl_6, 98%), lithium chloride (LiCl, 99%), and sulfuric acid (H_2SO_4, 95.0-98.0%) were purchased from Sigma–Aldrich. Commercial C/Pt (platinum, nominally 20% on carbon black) was obtained from Thermo Fisher Scientific. Cesium iodide (CsI) and rubidium iodide (RbI) were purchased from Sigma–Aldrich. Methylammonium bromide (MABr) and formamidinium iodide (FAI) were purchased from GreatCell Solar. Lead iodide (PbI_2) and lead bromide ($PbBr_2$) were purchased from TCI Chemicals. Anhydrous ethanol (EtOH), methanol (MeOH), dimethylformamide (DMF), and dimethyl sulfoxide (DMSO) were purchased from Sigma–Aldrich. [2-(3,6-Dimethoxy-9H-carbazol-9-yl)ethyl]phosphonic acid (MeO-2PACz), used as a hole transporting layer (HTL), was purchased from TCI Chemicals. C_{60} and bathocuproine (BCP), used as electron transport later (ETL), were purchased from Ossila and Lumtec, respectively. Self-adhesive graphite sheets were purchased from RS Components. Two types of graphite sheets were used: a 25 μm-thick sheet (designated as G3, density = 1.9 g cm^{-3}) and a 160 μm-thick sheet (designated as G15, density = 1.2 g cm^{-3}). All materials were used without any further purification.

4.2 | Synthesis of $C_{ZIF\text{-}8}$/Pt Catalyst

A total of 5 mmol of $Zn(NO_3)_2{\cdot}6H_2O$ was dissolved in 75 mL of methanol. Separately, 40 mmol of 2MIM was dissolved in another 75 mL of methanol. The 2MIM solution was rapidly poured into the $Zn(NO_3)_2$ solution under constant stirring. The resulting mixture was stirred for 2 h and aged still for 24 h. The milky suspension was centrifuged and washed three times with methanol. The resulting ZIF-8 was then dried at 70°C overnight. For the addition of Pt, 200 mg of the as-prepared ZIF-8 was dispersed in 20 mL of 0.2 M aniline aqueous solution. Then, different volumes of H_2PtCl_6 8 wt.% aqueous solution (50, 100, 250, and 500 μL) were added to the dispersion and stirred for 24 h. The resulting purple precipitates were centrifuged and washed three times with deionized water, followed by drying at 80°C overnight. To obtain the corresponding catalysts, 300 mg of each ZIF-8/Pt/aniline was carbonized at 1100°C for 2 h under a nitrogen atmosphere (Zn vaporizes at this temperature, unlike carbon and Pt). The aniline and final carbonized samples were named ZIF-8/Pt-aniline-*x*% and $C_{ZIF\text{-}8}$/Pt-*x*%, respectively, where *x* corresponds to the Pt content in the final $C_{ZIF\text{-}8}$/Pt carbonized samples. $C_{ZIF\text{-}8}$ was also prepared following the same procedure as in the $C_{ZIF\text{-}8}$/Pt samples, without the Pt-aniline addition.

4.3 | Preparation of G15/$C_{ZIF\text{-}8}$/Pt

For the fabrication of G15/$C_{ZIF\text{-}8}$/Pt, a catalyst ink was prepared by dispersing 5 mg of $C_{ZIF\text{-}8}$/Pt composite in a mixed solvent containing 0.5 mL of EtOH, 0.48 mL of DI water, and 0.02 mL of 5 wt.% Aquivion aqueous solution. The mixture was sonicated for 10 min to ensure uniform dispersion. The resulting suspension was drop-casted onto a ~150 μm-thick self-adhesive graphite sheet (labelled G15). For benchmarking, a commercial 20%wt. Pt supported on carbon (labelled C/Pt) was also applied with the same mixture loading including solvents and Aquivion to G15, resulting in G15/C/Pt. In both G15/$C_{ZIF\text{-}8}$/Pt and G15/C/Pt, the loading of carbon and Pt mixture on G15 was 0.318 mg cm^{-2}. A carbon-free sample (G15/Pt) was additionally prepared. A G15 graphite sheet was cut into a 1 × 3 cm piece, with a 1 × 1 cm area designated for Pt electrodeposition. Prior to Pt deposition, the graphite sheet was electrochemically activated in 0.5 M H_2SO_4 using a three-electrode configuration consisting of a KCl-saturated Ag/AgCl reference electrode and a Pt counter electrode. Activation was carried out by applying 10 cycle voltammetry sweeps between −0.3 and + 2.0 V (vs. Ag/AgCl). The activated graphite sheet was then rinsed with DI water and dried. For the Pt deposition step, the same three-electrode setup was used, and an aqueous solution was prepared by dissolving 1.43 × 10^{-3} M K_2PtCl_6 and 66 × 10^{-3} M LiCl in DI water. Then, Pt was electrodeposited potentiostatically at −0.5 V (vs. Ag/AgCl) until a charge of 128 mC cm^{-2} was reached. After deposition, the G15/Pt was washed with DI water and dried.

4.4 | Fabrication of Solar Cells

Perovskite solar cells were fabricated in an inverted p–i–n structure on glass substrates pre-patterned with indium tin oxide (ITO). The substrates were cleaned by sequential ultrasonication in acetone and isopropanol (IPA) for 10 min each, followed by nitrogen drying and a 20-min UV-ozone treatment. The HTL was applied by spin-coating a 0.75 mg mL^{-1} solution of MeO-2PACz in ethanol onto the substrates at 3000 rpm for 30 s inside a nitrogen-filled glovebox. The films were then annealed at 100°C for 10 min. For the perovskite active layer, a precursor solution of $Rb_{0.05}Cs_{0.05}MA_{0.05}FA_{0.85}Pb(I_{0.95}Br_{0.05})_3$ was prepared by dissolving CsI (19.5 mg), RbI (15.9 mg), MABr (8.4 mg), FAI (219.5 mg), PbI_2 (656.9 mg), and $PbBr_2$ (27.5 mg) in 1 mL of a DMF:DMSO solvent mixture (4:1 volume ratio). The solution was stirred at room temperature for 3–4 h. The perovskite layer was deposited using a two-step spin-coating process: first at 1000 rpm for 10 s, then at 3000 rpm for 40 s. After 20 s into the second spin step, 150 μL of chlorobenzene was dropped onto the spinning substrate as an antisolvent. The films were then annealed at 100°C for 10 min. To complete the device, 30 nm of C_{60}, 7 nm of BCP, and 100 nm of Ag were sequentially deposited via thermal evaporation. The active area of each device was defined as 0.64 cm^2.

4.5 | Preparation of IPV-Cathode

To fabricate the IPV-cathode, a self-adhesive graphite sheet (25 μm-thick, designated as G3) was first applied onto the Ag contact area of the solar cell. The thinness of the adhesive layer and the roughness of the graphite sheet ensures Ohmic contact between the Ag and graphite layers [91]. G3 has higher density relative to G15 (1.9 vs. 1.2 g cm^{-3}). The prepared G15/$C_{ZIF\text{-}8}$/Pt sheet was then applied on the G3 sheet to complete the monolithic perovskite IPV-cathode containing the full stack of glass/ITO/MeO-2PACz/$Rb_{0.05}Cs_{0.05}MA_{0.05}FA_{0.85}Pb(I_{0.95}Br_{0.05})_3$/$C_{60}$/BCP/Ag/G3-/G15/$C_{ZIF\text{-}8}$/Pt. To ensure a stable electrical connection to the potentiostat, copper foil was attached to the exposed ITO region of the device and Ag paste was applied. For benchmarking, a commercial 20%wt. Pt supported on carbon (labelled C/Pt) was also applied with the same mixture loading including solvents and Aquivion to G15 and employed to build an IPV-cathode.

4.6 | Characterization

The morphology of electrocatalysts was studied using scanning electron microscopy (SEM, Zeiss Sigma 300, Carl Zeiss, Germany) and transmission electron microscopy (TEM, JEOL 2100F, JEOL Ltd., Japan). For quantifying the Pt content, the carbon and platinum mixtures were prepared with mixed acid solution containing 2% HNO_3 and 1% HCl, and analyzed using ICP-MS (7900 ICP-MS, Agilent Technologies, USA). A Fourier-transform infrared spectroscopy (FT-IR, Spectrum 100, Perkin Elmer, USA) was employed to investigate functional groups of electrocatalysts and their precursors. The crystal structures were analyzed using x-ray diffraction (XRD, Aeris Benchtop, Malvern PANalytical) at a scan rate of 2° min^{-1} in the 2θ range of 10°–80° using Cu K_α radiation. Raman spectra were collected using a spectrometer (LabRam Aramis, Horiba Jobin Yvon, Japan) fitted with a 532 nm laser. The surface area and porosity were analyzed using N_2 sorption isotherm analysis (BELSORP-mini 11, MicrotracBEL, Japan). The specific surface area was determined using the Brunauer-Emmett-Teller (BET) model, while the pore size distribution using the non-local density functional theory (NLDFT) model on the adsorption isotherm. The chemical states and surface elemental compositions were analyzed using x-ray photoelectron spectroscopy (XPS, K-Alpha, Thermo Fisher Scientific, UK). The morphological and compositional changes in the catalysts after the durability test were investigated using SEM-EDS and TEM-EDS elemental mapping. ICP-MS analysis of the electrolyte was performed to quantify Pt dissolution during the stability test.

The perovskite layer was characterized by UV–vis spectroscopy, Kelvin probe (KP), and ambient photoemission spectroscopy (APS). UV–vis absorption spectra of glass/perovskite samples were measured using an Agilent Cary 60 UV–vis spectrophotometer. The work function (Fermi level) and ionization energy (valence band edge) of the perovskite were determined using a KP Technology SKP5050 Scanning Kelvin Probe and an APS02 Air Photoemission System, respectively, on glass/ITO substrates. These results were used to build the energy diagram, together with the well-known values of the rest of components taken from literature [92].

4.7 | Electrochemical and Photoelectrochemical Measurements

The electrochemical performances of the catalysts were measured in a three-electrode configuration using a potentiostat Solartron ModuLab XM ECS system, with a KCl-saturated Ag/AgCl electrode as the reference electrode, a Pt wire as the counter electrode, and 0.5 M H_2SO_4 as the electrolyte. For measurements without the effect of mass transfer resistance, the catalyst ink was directly loaded on a rotating disk electrode (RDE, 5 mm in diameter) terminated with glassy carbon and rotated at 2,500 rpm. For static measurements like those in IPV-cathodes (where mass transfer resistance occurs), the G15/$C_{ZIF\text{-}8}$/Pt was mounted on a vertical glass substrate. The carbon/Pt mixture loading was fixed at 0.318 mg cm^{-2}. All measured potentials were converted to the reversible hydrogen electrode (V_{RHE}) scale using the equation:

$$E_{RHE} = E_{Ag/AgCl} + 0.0592 \times pH + E^{o}_{Ag/AgCl} \quad (1)$$

where $E^{o}_{Ag/AgCl}$, is the potential of the reference electrode vs. the standard hydrogen electrode, which is 0.1976 V. Linear-sweep voltammetry (LSV) was conducted between + 0.1 and −0.6 V_{RHE} at a scan rate of 10 mV s^{-1}. Cyclic voltammetry (CV) was performed between + 0.5 and + 0.6 V_{RHE} at scan rates of 5, 10, 15, 20, and 25 mV s^{-1}. Additional CV measurements were conducted in the potential range of + 0.05 to + 0.7 V_{RHE} at a scan rate of 50 mV s^{-1}. Chronopotentiometry was carried out at a fixed current density of 20 mA cm^{-2}.

Current density–voltage (*J–V*) characteristics of the solar cell were measured using Ivium Compacstat potentiostat under simulated AM1.5G illumination (100 mW cm^{-2}) provided by a Lot Quantum Design xenon lamp. The light intensity was calibrated using a certified Internal Light Technologies SEL623 photodetector. For stability evaluation of the solar cell, chronoamperometry were performed at a potential of + 0.2 V. All measurements were carried out in ambient air. Standard error was calculated and represented with the symbol ±.

The IPV-cathode performance was evaluated using Ivium Compacstat potentiostat in a three-electrode setup, identical to the setup employed for electrochemical measurements under mass transfer resistance. Lot Quantum Design xenon lamp with an AM1.5G filter was used as the illumination source, and the light intensity was fixed at 1sun (100 mW cm^{-2}), calibrated with a certified International Light Technologies SEL623 photodetector. The open circuit potential (OCP) of the IPV-cathode was measured at 0 V_{RHE} under illumination for 30 s, followed by a dark period of 30 s, and the potential difference between the illuminated and dark states was defined as ΔOCP. LSV was carried out under both dark and illuminated conditions in the potential range from + 1.4 to −0.2 V_{RHE} at a scan rate of 10 mV s^{-1}. Chopped light measurement was performed with light periodically switched on and off at every 0.04 V interval, using a scan rate of 20 mV s^{-1}. For IPV-cathode stability evaluation, chronoamperometry was conducted at a fixed potential of 0 V_{RHE}. To evaluate the electrical resistance across interfaces, two-probe I–V measurements were performed on various architectures comprising FTO, Ag, G3, G15, C/Pt-19.3%, and $C_{ZIF\text{-}8}$/Pt-1.8%, using an Ivium Compacstat

potentiostat. The resistance (R) was determined according to Ohm's law, $R = \frac{V}{I}$, where V is the voltage and I is the current.

Author Contributions

Na Yeong Oh: conceptualization, writing – review and editing, investigation, writing – original draft, formal analysis, visualization. **Woo Jin Mun**: conceptualization, writing – review and editing, investigation, writing – original draft, formal analysis, visualization. **Kamran Dastafkan**: conceptualization, investigation, formal analysis. **Matyas Daboczi**: investigation, conceptualization, formal analysis. **Hongki Kim**: investigation. **Humza Bhatti**: investigation. **Eunyoung Hong**: investigation. **Minzhi Chen**: investigation. **Yongqi Huang**: investigation. **Jin Hyuk Kim**: investigation. **Nicola Gasparini**: investigation, conceptualization, supervision, writing – review and editing, formal analysis. **Jong Hak Kim**: funding acquisition, conceptualization, investigation, writing – review and editing, supervision, project administration, formal analysis. **Salvador Eslava**: investigation, conceptualization, funding acquisition, writing – original draft, writing – review and editing, visualization, formal analysis, project administration, supervision.

Funding

N.Y.O. and W.J.M. acknowledge support from the Korea Institute of Energy Technology Evaluation and Planning (KETEP) funded by the Korea government (MOTIE) (RS-2024-00487069). K.D., M.D., and S.E. acknowledge the funding of UK Engineering and Physical Sciences Research Council provided via grant nos. EP/S030727/1. M.D. also acknowledges support received from the European Union under the Marie Skłodowska-Curie Actions grant agreement no. 101103762.

Conflicts of Interest

The authors declare no conflicts of interest.

Data Availability Statement

The data that support the findings of this study are openly available in the following Figshare data repository at DOI: https://doi.org/10.6084/m9.figshare.32789934.

References

1. L. Clarizia, M. N. Nadagouda, and D. D. Dionysiou, "Recent Advances and Challenges of Photoelectrochemical Cells for Hydrogen Production," *Current Opinion in Green and Sustainable Chemistry* 41 (2023): 100825.

2. Y. Zhao, Z. Niu, J. Zhao, L. Xue, X. Fu, and J. Long, "Recent Advancements in Photoelectrochemical Water Splitting for Hydrogen Production," *Electrochemical Energy Reviews* 6 (2023): 14.

3. N.-G. Park, "Perovskite Solar Cells: An Emerging Photovoltaic Technology," *Materials Today* 18 (2015): 65–72.

4. Q. Ou, X. Bao, Y. Zhang, et al., "Band Structure Engineering in Metal Halide Perovskite Nanostructures for Optoelectronic Applications," *Nano Materials Science* 1 (2019): 268–287.

5. S. D. Stranks, G. E. Eperon, G. Grancini, et al., "Electron-Hole Diffusion Lengths Exceeding 1 Micrometer in an Organometal Trihalide Perovskite Absorber," *Science* 342 (2013): 341–344.

6. H. Zhu, S. Teale, M. N. Lintangpradipto, et al., "Long-Term Operating Stability in Perovskite Photovoltaics," *Nature Reviews Materials* 8 (2023): 569–586.

7. A. M. K. Fehr, A. Agrawal, F. Mandani, et al., "Integrated Halide Perovskite Photoelectrochemical Cells With Solar-Driven Water-Splitting Efficiency of 20.8%," *Nature Communications* 14 (2023): 3797.

8. J. Park, J. Lee, H. Lee, et al., "Hybrid Perovskite-Based Wireless Integrated Device Exceeding a Solar to Hydrogen Conversion Efficiency of 11%," *Small* 19 (2023): 2300174.

9. V. Andrei, R. L. Z. Hoye, M. Crespo-Quesada, et al., "Scalable Triple Cation Mixed Halide Perovskite–$BiVO_4$ Tandems for Bias-Free Water Splitting," *Advanced Energy Materials* 8 (2018): 1801403.

10. M. Crespo-Quesada, L. M. Pazos-Outón, J. Warnan, M. F. Kuehnel, R. H. Friend, and E. Reisner, "Metal-Encapsulated Organolead Halide Perovskite Photocathode for Solar-Driven Hydrogen Evolution in Water," *Nature Communications* 7 (2016): 12555.

11. J.-H. Kim, S. Seo, J.-H. Lee, et al., "Efficient and Stable Perovskite-Based Photocathode for Photoelectrochemical Hydrogen Production," *Advanced Functional Materials* 31 (2021): 2008277.

12. J. Yun, Y. S. Park, H. Lee, et al., "Efficient and Ultrastable Iodide Oxidation Reaction Over Defect-Passivated Perovskite Photoanode for Unassisted Solar Fuel Production," *Advanced Energy Materials* 14 (2024): 2401055.

13. T. G. Kim, J. H. Lee, G. Hyun, et al., "Monolithic Lead Halide Perovskite Photoelectrochemical Cell with 9.16% Applied Bias Photon-to-Current Efficiency," *ACS Energy Letters* 7 (2022): 320–327.

14. C. Pornrungroj, V. Andrei, M. Rahaman, et al., "Bifunctional Perovskite-$BiVO_4$ Tandem Devices for Uninterrupted Solar and Electrocatalytic Water Splitting Cycles," *Advanced Functional Materials* 31 (2021): 2008182.

15. V. Andrei, G. M. Ucoski, C. Pornrungroj, et al., "Floating Perovskite-$BiVO_4$ Devices for Scalable Solar Fuel Production," *Nature* 608 (2022): 518–522.

16. M. Daboczi, J. Cui, F. Temerov, and S. Eslava, "Scalable All-Inorganic Halide Perovskite Photoanodes with >100 h Operational Stability Containing Earth-Abundant Materials," *Advanced Materials* 35 (2023): 2304350.

17. Z. Zhu, M. Daboczi, M. Chen, Y. Xuan, X. Liu, and S. Eslava, "Ultrastable Halide Perovskite $CsPbBr_3$ Photoanodes Achieved With Electrocatalytic Glassy-Carbon and Boron-Doped Diamond Sheets," *Nature Communications* 15 (2024): 2791.

18. I. Poli, U. Hintermair, M. Regue, et al., "Graphite-Protected $CsPbBr_3$ Perovskite Photoanodes Functionalised With Water Oxidation Catalyst for Oxygen Evolution in Water," *Nature Communications* 10 (2019): 2097.

19. M. Yasin, N. Khan, M. Murad, et al., "Pt-Based Electrocatalyst for Hydrogen Evolution in Acidic Electrolytes," *Electrochemistry Communications* 180 (2025): 108057.

20. J. N. Tiwari, S. Sultan, C. W. Myung, et al., "Multicomponent Electrocatalyst With Ultralow Pt Loading and High Hydrogen Evolution Activity," *Nature Energy* 3 (2018): 773–782.

21. J. Li, H.-X. Liu, W. Gou, et al., "Ethylene-Glycol Ligand Environment Facilitates Highly Efficient Hydrogen Evolution of Pt/CoP Through Proton Concentration and Hydrogen Spillover," *Energy & Environmental Science* 12 (2019): 2298–2304.

22. Z. W. Seh, J. Kibsgaard, C. F. Dickens, I. Chorkendorff, J. K. Nørskov, and T. F. Jaramillo, "Combining Theory and Experiment in Electrocatalysis: Insights Into Materials Design," *Science* 355 (2017): aad4998.

23. J. Kibsgaard and I. Chorkendorff, "Considerations for the Scaling-Up of Water Splitting Catalysts," *Nature Energy* 4 (2019): 430–433.

24. F. Guo, T. J. Macdonald, A. J. Sobrido, L. Liu, J. Feng, and G. He, "Recent Advances in Ultralow-Pt-Loading Electrocatalysts for the Efficient Hydrogen Evolution," *Advanced Science* 10 (2023): 2301098.

25. J. N. Hansen, H. Prats, K. K. Toudahl, et al., "Is There Anything Better than Pt for HER?," *ACS Energy Letters* 6 (2021): 1175–1180.

26. E. Kemppainen, A. Bodin, B. Sebok, et al., "Scalability and Feasibility of Photoelectrochemical H_2 Evolution: The Ultimate Limit of Pt

Nanoparticle as an HER Catalyst," *Energy & Environmental Science* 8 (2015): 2991–2999.

27. D. Liu, X. Li, S. Chen, et al., "Atomically Dispersed Platinum Supported on Curved Carbon Supports for Efficient Electrocatalytic Hydrogen Evolution," *Nature Energy* 4 (2019): 512–518.

28. L. Liu, Y. Wang, Y. Zhao, et al., "Ultrahigh Pt-Mass-Activity Hydrogen Evolution Catalyst Electrodeposited From Bulk Pt," *Advanced Functional Materials* 32 (2022): 2112207.

29. D. Jin, F. Qiao, H. Chu, and Y. Xie, "Progress in Electrocatalytic Hydrogen Evolution of Transition Metal Alloys: Synthesis, Structure, and Mechanism Analysis," *Nanoscale* 15 (2023): 7202–7226.

30. Z. Liu, J. Qi, M. Liu, et al., "Aqueous Synthesis of Ultrathin Platinum/Non-Noble Metal Alloy Nanowires for Enhanced Hydrogen Evolution Activity," *Angewandte Chemie International Edition* 57 (2018): 11678–11682.

31. J. Li, M. N. Banis, Z. Ren, et al., "Unveiling the Nature of Pt Single-Atom Catalyst during Electrocatalytic Hydrogen Evolution and Oxygen Reduction Reactions," *Small* 17 (2021): 2007245.

32. C. Yue, C. Feng, G. Sun, et al., "Hierarchically Stabilized Pt Single-Atom Catalysts Induced by an Atomic Substitution Strategy for an Efficient Hydrogen Evolution Reaction," *Energy & Environmental Science* 17 (2024): 5227–5240.

33. T. Chu, G. Wang, X. Zhang, et al., "High-Density Dual-Structure Single-Atom Pt Electrocatalyst for Efficient Hydrogen Evolution and Multimodal Sensing," *Nano Letters* 24 (2024): 9666–9674.

34. D. K. K. Kori, R. G. Jadhav, L. Dhruv, and A. K. Das, "A platinum Nanoparticle Doped Self-Assembled Peptide Bolaamphiphile Hydrogel as an Efficient Electrocatalyst for the Hydrogen Evolution Reaction," *Nanoscale Advances* 3 (2021): 6678–6688.

35. A. Shan, X. Teng, Y. Zhang, et al., "Interfacial Electronic Structure Modulation of Pt-MoS_2 Heterostructure for Enhancing Electrocatalytic Hydrogen Evolution Reaction," *Nano Energy* 94 (2022): 106913.

36. K. L. Zhou, Z. Wang, C. B. Han, et al., "Platinum Single-Atom Catalyst Coupled With Transition Metal/Metal Oxide Heterostructure for Accelerating Alkaline Hydrogen Evolution Reaction," *Nature Communications* 12 (2021): 3783.

37. M. Lao, K. Rui, G. Zhao, et al., "Platinum/Nickel Bicarbonate Heterostructures Towards Accelerated Hydrogen Evolution Under Alkaline Conditions," *Angewandte Chemie International Edition* 58 (2019): 5432–5437.

38. Y. Li, K. Jiang, J. Yang, et al., "Tungsten Oxide/Reduced Graphene Oxide Aerogel with Low-Content Platinum as High-Performance Electrocatalyst for Hydrogen Evolution Reaction," *Small* 17 (2021): 2102159.

39. H. Hong, H. Y. Kim, W. I. Cho, et al., "Surface-Functionalized Three-Dimensional MXene Supports to Boost the Hydrogen Evolution Activity of Pt Catalysts in Alkaline Media," *Journal of Materials Chemistry A* 11 (2023): 5328–5336.

40. J. Zhang, Y. Zhao, X. Guo, et al., "Single Platinum Atoms Immobilized on an MXene as an Efficient Catalyst for the Hydrogen Evolution Reaction," *Nature Catalysis* 1 (2018): 985–992.

41. J. Sun, Z. Zhang, and X. Meng, "Low-Pt Supported on MOF-Derived $Ni(OH)_2$ With Highly-Efficiently Electrocatalytic Seawater Splitting at High Current Density," *Applied Catalysis B: Environmental* 331 (2023): 122703.

42. C. Zhang, P. Wang, W. Li, et al., "MOF-Assisted Synthesis of Octahedral Carbon-Supported PtCu Nanoalloy Catalysts for an Efficient Hydrogen Evolution Reaction," *Journal of Materials Chemistry A* 8 (2020): 19348–19356.

43. J. Li, H. Huang, Y. Li, Y. Tang, D. Mei, and C. Zhong, "Stable and size-Controllable Ultrafine Pt nanoparticles Derived From a MOF-Based Single Metal Ion Trap for Efficient Electrocatalytic Hydrogen Evolution," *Journal of Materials Chemistry A* 7 (2019): 20239–20246.

44. M. Kim, R. Xin, J. Earnshaw, et al., "MOF-Derived Nanoporous Carbons With Diverse Tunable Nanoarchitectures," *Nature Protocols* 17 (2022): 2990–3027.

45. H. Laeim, V. Molahalli, P. Prajongthat, et al., "Porosity Tunable Metal-Organic Framework (MOF)-Based Composites for Energy Storage Applications: Recent Progress," *Polymers* 17 (2025): 130.

46. X. Xia, J. Liu, Y. Xiao, et al., "Superhydrophobic Acid-Resistant Fluorinated Zif-8 Prepared at Normal Temperature and Pressure," *Chemical Engineering Journal* 505 (2025): 159223.

47. H. Yin, H. Kim, J. Choi, and A. C. K. Yip, "Thermal Stability of ZIF-8 Under Oxidative and Inert Environments: A Practical Perspective on Using ZIF-8 as a Catalyst Support," *Chemical Engineering Journal* 278 (2015): 293–300.

48. S. Penukula, F. Tippin, M. Li, K. A. Khawaja, F. Yan, and N. Rolston, "Use of Carbon Electrodes to Reduce Mobile Ion Concentration and Improve Reliability of Metal Halide Perovskite Photovoltaics," *Energy Materials* 4 (2024): 400060.

49. S. Yun, Z. Gao, T. Yang, et al., "Constructing $NiSe_2$ /$MoSe_2$ Mott–Schottky Heterojunctions Onto N-Doped Brain Coral-Carbon Spheres by Phase Separation Strategies for Advanced Energy Conversion Applications," *Advanced Functional Materials* 34 (2024): 2314226.

50. H. Yang, S. Yun, T. Yang, et al., "Entropy-Assisted Nitrogen-Doped Carbon-Anchored High-Entropy Alloy Composites for Efficient and Stable Universal Photovoltaic Electrodes," *Journal of Materials Chemistry A* 14 (2026): 15297–15310.

51. T. Yang, M. Sun, Q. Pang, et al., "Phase-Segregation Engineering of Binary Metal Selenide Heterojunctions on 3D N-Doped Carbon Cubes: Boosting Carrier Transport via Electron-Rich Field for High-Performance Photovoltaics," *Advanced Functional Materials* 36 (2026): 31713.

52. X. Xu, S. Yun, G. Yang, et al., "Oxygen Vacancy-Mediated 3D/2D Hydrange-Type Bismuth Oxides with 1D Bi_2Se_3 Nanowires Confined via a Mild Selenization Strategy to Trigger Dual Built-in Electric Fields for Accelerated Energy Conversion," *Advanced Functional Materials* 35 (2025): 2504278.

53. Y. Tong, X. Yu, H. Wang, B. Yao, C. Li, and G. Shi, "Trace Level Co–N Doped Graphite Foams as High-Performance Self-Standing Electrocatalytic Electrodes for Hydrogen and Oxygen Evolution," *ACS Catalysis* 8 (2018): 4637–4644.

54. Y. Oh, B. N. Vamsi Krishna, H. J. Jung, A. Toor, and S. J. Lee, "Rhodium Nanoparticle-Supported Graphitic Carbon-Encapsulated Nickel Metal Core Electrocatalyst via Pulsed Laser Ablation for Hydrogen Evolution Reaction," *ACS Applied Materials & Interfaces* 17 (2025): 44402.

55. J. Wang, W. Zang, X. Liu, et al., "Switch Volmer-Heyrovsky to Volmer-Tafel Pathway for Efficient Acidic Electrocatalytic Hydrogen Evolution by Correlating Pt Single Atoms with Clusters," *Small* 20 (2024): 2309427.

56. D. Zhang, Z. Wang, X. Wu, et al., "Noble Metal (Pt, Rh, Pd, Ir) Doped Ru/CNT Ultra-Small Alloy for Acidic Hydrogen Evolution at High Current Density," *Small* 18 (2022): 2104559.

57. P. Gozali Balkanloo, A. Poursattar Marjani, and M. Mahmoudian, "Fabrication, Characterization, and Performance Evaluation of Polysulfone Nanocomposite Membranes Containing Different Sizes of ZIF-8 to Desalination and Heavy Metals Removal From Wastewater," *Chemical Engineering Journal* 496 (2024): 153835.

58. S. Menon, S. Dutta, N. Madaboosi, and V. V. R. Sai, "Cobalt-Doped ZIF-8 Nanoparticle-Decorated Fiber Optic Sensor for Copper Ion Detection," *ACS Applied Nano Materials* 7 (2024): 18346.

59. M. Ilic, E. Koglin, A. Pohlmeier, H. D. Narres, and M. J. Schwuger, "Adsorption and Polymerization of Aniline on Cu(II)-Montmorillonite: Vibrational Spectroscopy and ab Initio Calculation," *Langmuir* 16 (2000): 8946–8951.

60. Z. D. Zujovic and J. B. Metson, "Nanostructured Aniline Oxidation Products: Self-Assembled Films at the Air/Liquid Interface," *Langmuir* 27 (2011): 7776–7782.

61. P. Zhang, F. Sun, Z. Xiang, Z. Shen, J. Yun, and D. Cao, "ZIF-Derived In Situ Nitrogen-Doped Porous Carbons as Efficient Metal-Free Electrocatalysts for Oxygen Reduction Reaction," *Energy & Environmental Science* 7 (2014): 442–450.

62. Z. Abbasi, E. Shamsaei, S. K. Leong, B. Ladewig, X. Zhang, and H. Wang, "Effect of Carbonization Temperature on Adsorption Property of ZIF-8 Derived Nanoporous Carbon for Water Treatment," *Microporous and Mesoporous Materials* 236 (2016): 28–37.

63. W. Zhu, S. Zhang, X. Zuo, et al., "ZIF-8-Derived Nitrogen-Doped Porous Carbon Supported $CuFeO_2$ for Sulfamethoxazole Removal: Performances, Degradation Pathways and Mechanisms," *Journal of Environmental Chemical Engineering* 11 (2023): 109587.

64. L. M. Esteves, T. J. Ferreira, A. Keba, J. M. S. S. Esperança, and I. A. A. C. Esteves, "Carbon Materials Derived From Cyano-Based IL@ZIF-8 Composites for CO_2 Sorption Separation Systems," *Materials Today Sustainability* 22 (2023): 100353.

65. U. Y. Lee, D. I. Jeong, J. S. Ha, et al., "Fine-Tunable N-Doping in Carbon-Coated CoFe Nano-Cubes for Efficient Hydrogen Evolution in AEM Water Electrolysis," *Advanced Composites and Hybrid Materials* 8 (2025): 140.

66. X. Luo, P. Yuan, H. Xiao, et al., "Effects of Intrinsic Defects in Pt-Based Carbon Supports on Alkaline Hydrogen Evolution Reaction," *ACS Applied Materials & Interfaces* 16 (2024): 26044–26056.

67. S. Eslava, M. R. Baklanov, A. V. Neimark, et al., "Evidence of Large Voids in Pure-Silica-Zeolite Low- k Dielectrics Synthesized by Spin-On of Nanoparticle Suspensions," *Advanced Materials* 20 (2008): 3110–3116.

68. L. Zhang, Z. Su, F. Jiang, et al., "Highly Graphitized Nitrogen-Doped Porous Carbon Nanopolyhedra Derived From ZIF-8 Nanocrystals as Efficient Electrocatalysts for Oxygen Reduction Reactions," *Nanoscale* 6 (2014): 6590–6602.

69. G. Zhu, L. Ma, H. Lv, et al., "Pine Needle-Derived Microporous Nitrogen-Doped Carbon Frameworks Exhibit High Performances in Electrocatalytic Hydrogen Evolution Reaction and Supercapacitors," *Nanoscale* 9 (2017): 1237–1243.

70. J. Zhang, Z. Wan, X. Bu, et al., "Electronic Interaction Enables Pt Nanoparticles on N-Doped Porous Carbon Aerogel as Efficient Electrocatalysts for Alkaline Hydrogen Evolution Reaction," *Small* 21 (2025): 06453.

71. H. Zhang, H. Li, X. Zhang, S. Yu, S. Wang, and G. Sun, "Enhanced Metal-Support Interaction of Nitrogen-Doped Carbon Supported Pt Nanoparticles With High Activity for Electrocatalytic Oxygen Reduction Reaction," *Carbon Neutrality* 4 (2025): 10.

72. M. Daboczi, F. Eisner, J. Luke, et al., "Enhanced Solar Water Oxidation and Unassisted Water Splitting Using Graphite-Protected Bulk Heterojunction Organic Photoactive Layers," *Nature Energy* 10 (2025): 581–591.

73. C. Chen, S. Zhang, S. Wu, et al., "Effect of BCP Buffer Layer on Eliminating Charge Accumulation for High Performance of Inverted Perovskite Solar Cells," *RSC advances* 7 (2017): 35819.

74. C. L. Do, T. S. Pham, N. P. Nguyen, and V. Q. Tran, "Properties of Pt/C Nanoparticle Catalysts Synthesized by Electroless Deposition for Proton Exchange Membrane Fuel Cell," *Advances in Natural Sciences: Nanoscience and Nanotechnology* 4 (2013): 035011.

75. S. Prass, J. St-Pierre, M. Klingele, K. A. Friedrich, and N. Zamel, "Hydrogen Oxidation Artifact During Platinum Oxide Reduction in Cyclic Voltammetry Analysis of Low-Loaded PEMFC Electrodes," *Electrocatalysis* 12 (2021): 45–55.

76. M. V. Khenkin, E. A. Katz, A. Abate, et al., "Consensus statement for Stability Assessment and Reporting for Perovskite Photovoltaics Based on ISOS Procedures," *Nature Energy* 5 (2020): 35–49.

77. S. Khamgaonkar, Q. Chen, K. Musselman, and V. Maheshwari, "Stable Perovskite Photocathodes for Efficient Hydrogen Evolution in Acidic and Basic Conditions," *Journal of Materials Chemistry A* 11 (2023): 20079–20088.

78. H. Zhang, Z. Yang, W. Yu, et al., "A Sandwich-Like Organolead Halide Perovskite Photocathode for Efficient and Durable Photoelectrochemical Hydrogen Evolution in Water," *Advanced Energy Materials* 8 (2018): 1800795.

79. I. S. Kim, M. J. Pellin, and A. B. F. Martinson, "Acid-Compatible Halide Perovskite Photocathodes Utilizing Atomic Layer Deposited TiO_2 for Solar-Driven Hydrogen Evolution," *ACS Energy Letters* 4 (2019): 293–298.

80. L.-F. Gao, W.-J. Luo, Y.-F. Yao, and Z.-G. Zou, "An All-Inorganic Lead Halide Perovskite-Based Photocathode for Stable Water Reduction," *Chemical Communications* 54 (2018): 11459–11462.

81. S. Ahmad, A. Sadhanala, R. L. Z. Hoye, et al., "Triple-Cation-Based Perovskite Photocathodes with AZO Protective Layer for Hydrogen Production Applications," *ACS Applied Materials & Interfaces* 11 (2019): 23198–23206.

82. H. Choi, S. Seo, J.-H. Kim, et al., "An Organometal Halide Perovskite Photocathode Integrated With a MoS_2 Catalyst for Efficient and Stable Photoelectrochemical Water Splitting," *Journal of Materials Chemistry A* 9 (2021): 22291–22300.

83. D. Hansora, R. Mehrotra, E. Noh, et al., "Scalable and Durable Module-Sized Artificial Leaf With a Solar-To-Hydrogen Efficiency Over 10%," *Nature Communications* 16 (2025): 4186.

84. M. A. Mubarok, Y. Choi, R. Mehrotra, et al., "Efficient and Stable Tin–Lead Perovskite Photoconversion Devices Using Dual-Functional Cathode Interlayer," *Advanced Energy Materials* 14 (2024): 2302555.

85. A. Paracchino, V. Laporte, K. Sivula, M. Grätzel, and E. Thimsen, "Highly Active Oxide Photocathode for Photoelectrochemical Water Reduction," *Nature Materials* 10 (2011): 456–461.

86. S. S. Kalanur, Y. J. Lee, and H. Seo, "Enhanced and Stable Photoelectrochemical H_2 Production Using a Engineered Nano Multijunction With Cu_2O Photocathode," *Materials Today Chemistry* 26 (2022): 101031.

87. Y.-C. Chen, H.-Y. Yeh, R. Popescu, D. Gerthsen, and Y.-K. Hsu, "Solution–Processed $Cu_2O/ZnO/TiO_2$/Pt Nanowire Photocathode for Efficient Photoelectrochemical Water Splitting," *Journal of Alloys and Compounds* 899 (2022): 163348.

88. R. R. Prabhakar, W. Septina, S. Siol, T. Moehl, R. Wick-Joliat, and S. D. Tilley, "Photocorrosion-Resistant Sb_2Se_3 Photocathodes With Earth Abundant MoS_x Hydrogen Evolution Catalyst," *Journal of Materials Chemistry A* 5 (2017): 23139–23145.

89. D. Zhang, M. Du, P. Wang, et al., "Hole-Storage Enhanced A-Si Photocathodes for Efficient Hydrogen Production," *Angewandte Chemie International Edition* 60 (2021): 11966–11972.

90. X. Cheng, H. Shen, W. Dong, et al., "Nano-Au and Ferroelectric Polarization Mediated Si/ITO/$BiFeO_3$ Tandem Photocathode for Efficient H_2 Production," *Advanced Materials Interfaces* 3 (2016): 1600485.

91. S. Barg, F. M. Perez, N. Ni, et al., "Mesoscale assembly of Chemically Modified Graphene Into Complex Cellular Networks," *Nature Communications* 5 (2014): 4328.

92. E. Hong, W. D. J. Tremlett, L. Hart, et al., "Ferrocene Derivatives Enable Ultrasensitive Perovskite Photodetectors With Enhanced Reverse Bias Stability," *Advanced Functional Materials* 36 (2026): 2424556.

Supporting Information

Additional supporting information can be found online in the Supporting Information section.

Supporting File: adfm77308-sup-0001-SuppMat.pdf.